ACS OMEGA

Open Access

http://pubs.acs.org/journal/acsodf

Article

Theoretical Investigations of Substrate Behavior in $FeCl_3$-Catalyzed Carbonyl−Olefin Metathesis

Cory W. Schneider and James J. Devery, III*

Cite This: *ACS Omega* 2025, 10, 10283−10293

Read Online

ACCESS | Metrics & More | Article Recommendations | Supporting Information

ABSTRACT: $FeCl_3$-catalyzed ring-closing carbonyl−olefin metathesis is a powerful method for the formation of cyclic olefins. Multiple substrate classes are known to display this reactivity; however, two substrates have been reported to form an oxetane, and do not undergo retro-[2 + 2] fragmentation into the cyclic olefin and a byproduct carbonyl. Specifically, phenanthrene producing polycyclic aromatic hydrocarbons yield an oxetane when electrophilic fluorine is introduced α to the substrate carbonyl. Herein, we report the application of quantum chemical modeling of enthalpies and NBO charges to investigate this divergent reactivity. In particular, the replacement of C−H bonds with C−F bonds eliminates hyperconjugative stabilization of the retro-[2 + 2] transition state. Taken together, this model suggests that charge stabilization at the reactive carbonyl carbon dictates the ability of the oxetane to fragment into the metathesis product. However, we also observe that electron-deficient carbonyls have a significantly lower barrier to Fe(III)-mediated oxetane formation. Balancing the factors implicated by our model, we predict the structures of possible metathesis-active molecules as well as oxetane-forming molecules.

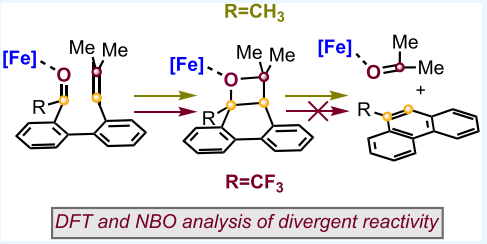

INTRODUCTION

Carbonyl−olefin metathesis as a process for the construction of high-value small molecules has seen increasing development over the past decade.[1] Methods facilitating this functional group exchange have developed using reagent systems which affect this transformation through parallel mechanistic pathways. Metal alkylidenes operate stoichiometrically via the formation of metallocyclobutanes and metallooxetanes.[2] Hydrazines operate as Lewis basic catalysts via pyrazolidines.[3] Activated olefins and carbonyls can be induced to form diols and undergo Grob fragmentations photocatalytically,[4] or with clay in flow.[5] Lastly, photochemically formed oxetanes, or those catalytically formed with Lewis acids, can be fragmented thermally or via exposure to Lewis acids.[6] It is this last group which has garnered the most attention.

Lewis acid-catalyzed carbonyl−olefin metathesis methods include ring-opening metathesis, cross metathesis, and the most well studied: ring-closing carbonyl−olefin metathesis.[1c] Particular attention has been dedicated to enumerating the Lewis acids capable of catalyzing the reactions, including clays,[5,7] trityl cation,[8] HCl via a host−guest interaction,[9] tropylium salts,[10] I_2,[11] $BF_3{\cdot}OEt_2$,[5] TsOH via a hexafluoroisopropanol hydrogen bonding network,[12] and metal halides featuring Ga(III),[13] Al(III),[14] Au(III),[15] and Fe(III).[16]

Working alongside the Schindler and Zimmerman laboratories, we have previously reported our efforts to elucidate the operating catalytic cycle of Lewis acid-catalyzed carbonyl−olefin metathesis when linear motifs like **1** are exposed to substoichiometric $FeCl_3$ in DCE (Figure 1A).[17] Carbonyl−olefin pair **1** forms Lewis pair **4** with the Fe(III)-center. This coordination induces turnover-limiting formation of oxetane **5** via an asynchronous [2 + 2]-cycloaddition. The still bound $FeCl_3$ then directs fragmentation of the oxetane via retro-[2 + 2]-cycloaddition, yielding cycloalkene **2**. Carbonyl exchange turns the catalyst over to the next molecule of **1**. This mechanism appears to explain the Lewis-acid catalyzed formation of styrenyl cyclopentenes and hexenes,[16a] styrenyl dihydropyrroles and styrenyl tetrahydropyridines,[16d,f] and polycyclic aromatic hydrocarbons.[16c] Importantly, this last group offers an isolated intermediate of our proposed carbonyl−olefin metathesis mechanism: an oxetane.

Schindler and co-workers reported that when biphenyl carbonyl−olefin pairs like **6** are exposed to substoichiometric $FeCl_3$ in toluene, phenanthrene **7** results (Figure 1B).[16c] Interestingly, the reaction in toluene halts early for biphenyl **8**, yielding oxetane **9**, which they characterized unambiguously. This Lewis acid-facilitated oxetane formation is consistent with the earlier work of Demole,[18] who reported a $SnCl_4$-mediated formation of **11** in nitromethane, and Coates,[19] who reported the $TiCl_4$-mediated formation of **13** in DCM (Figure 1C). Importantly, Schindler and co-workers reproduced Demole's oxetane using $FeCl_3$ in DCE,[16e] providing a second substrate that results in oxetane formation catalyzed by $FeCl_3$.[20] We believe this obstacle to metathesis success reported by

Received: October 29, 2024
Revised: February 14, 2025
Accepted: February 21, 2025
Published: March 6, 2025

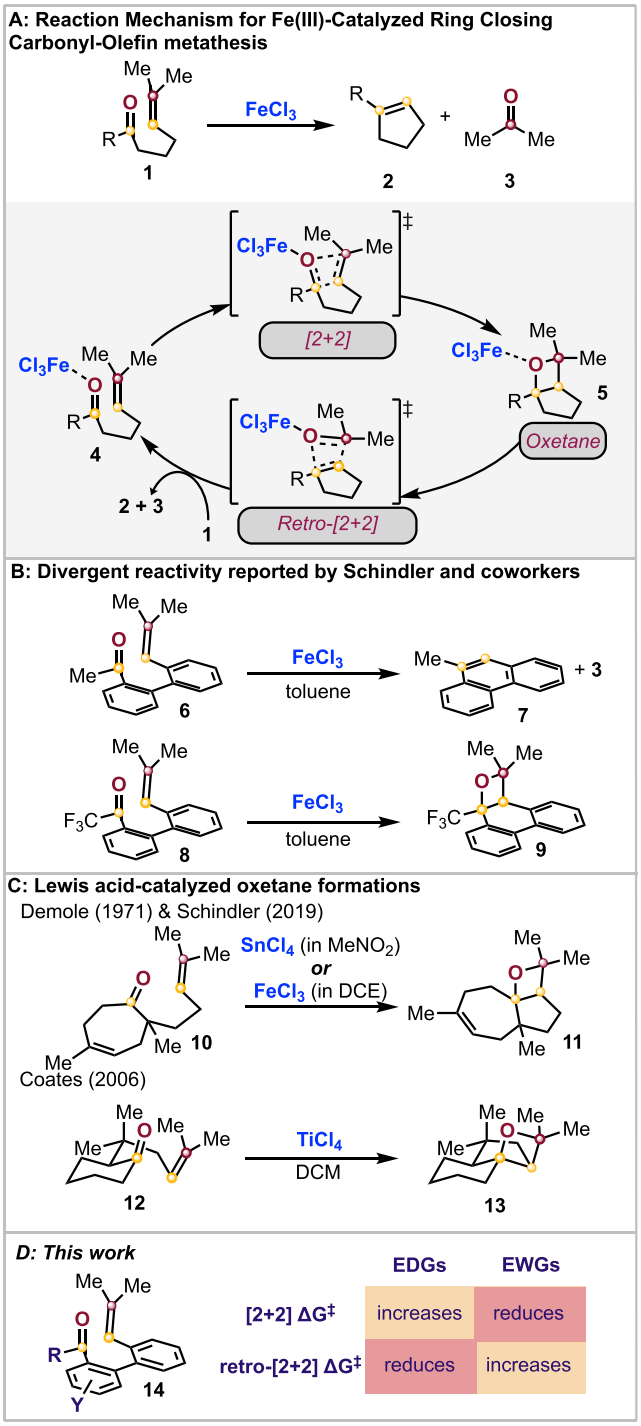

Figure 1. Substrate Behavior in Fe-Catalyzed carbonyl−olefin metathesis (A). Divergent reactivity reported by Schindler and coworkers (B). Examples of Lewis acid-mediated oxetane formation (C). Proposal for substrate behavior (D).

Schindler and co-workers offers an opportunity to discern how substrate structure contributes to Lewis acid-catalyzed carbonyl−olefin metathesis beyond structural changes that result in a complete negation of reactivity. Further, the biphenyl substrate motif offered the ability to examine not only the impact of the CF_3 group, but also the arene attached to the carbonyl.

Based on the $FeCl_3$-catalyzed synthetic results of the Schindler lab,[16c,e] we envisioned a systematic investigation of the reaction coordinate to achieve an understanding of the guiding principles of this transformation. Herein, we report an investigation of the role that substrate structure plays in the reaction coordinate of $FeCl_3$-catalyzed carbonyl−olefin metathesis. This investigation employs quantum chemical calculations to perform a theoretical Hammett analysis of the reaction coordinate. From this investigation, we determined that while the functionality of the aromatic ring adjacent to the carbonyl impacts the reaction, its impact is secondary to that of the addition of F atoms α to the carbonyl. In particular, we report how the changes to electronic structure correlate to reaction outcomes. This fundamental understanding of how structure impacts the reaction coordinate will promote the ability of synthetic chemists to expand the scope of carbonyl−olefin metathesis, as well as deliberately target the formation of oxetanes.

RESULTS AND DISCUSSION

Reaction Coordinate Analysis. We began our investigation by examining the DFT-simulated reaction pathways for both the methyl and trifluoromethyl systems (Figure 2). In particular, we wanted to apply the energy span model to our system in order to observe $\Delta G^{\ddagger}$ of each transition state.[21] For each system, there is a conformational shift from the lowest energy conformer ($\mathbf{15a_{Me}}$, $\mathbf{15a_{CF3}}$) to the reactive conformer ($\mathbf{15b_{Me}}$, $\mathbf{15b_{CF3}}$), resulting in an energy increase of 2.7 kcal/mol for the methyl system, and 3.2 kcal/mol for the trifluoromethyl system.[22] For the methyl system, from its reactive conformer, we see a cycloaddition transition state energy ($\Delta G_C^{\ddagger}$) of 13.6 kcal/mol for the transformation of $\mathbf{15b_{Me}}$ to $\mathbf{17_{Me}}$ through transition state $\mathbf{16_{Me}}$. For retro-cycloaddition transition state $\mathbf{18_{Me}}$, we see a higher energy ($\Delta G_{RC}^{\ddagger}$) of 13.9 kcal/mol for the transition of $\mathbf{17_{Me}}$ to $\mathbf{19_{Me}}$. For the trifluoromethyl system, we see an $\Delta G_C^{\ddagger}$ of 3.5 kcal/mol for the transformation of $\mathbf{15b_{CF3}}$ to $\mathbf{17_{CF3}}$ through transition state $\mathbf{16_{CF3}}$. For retro-cycloaddition transition state $\mathbf{18_{CF3}}$, we see a higher $\Delta G_{RC}^{\ddagger}$ of 21.1 kcal/mol for the transition of $\mathbf{17_{CF3}}$ to $\mathbf{19_{CF3}}$. There is a clear decrease in the cycloaddition energy requirement concurrently, with an increase in the retro-cycloaddition requirement when the trifluoro group is present relative to the methyl system. When we compare $\Delta G^{\ddagger}$ of $\mathbf{16_{Me}}$ to $\mathbf{18_{Me}}$ relative to their lowest energy conformers $\mathbf{15a_{Me}}$ and $\mathbf{17_{Me}}$, the methyl system's turnover-limiting transition state is the cycloaddition transition state $\mathbf{16_{Me}}$ (16.3 kcal/mol). The corresponding analysis in the trifluoromethyl system suggests that the turnover-limiting transition state is retro-cycloaddition $\mathbf{18_{CF3}}$ (21.1 kcal/mol). This difference is consistent with Schindler's empirical results, which suggest that this barrier is prohibitive. With this difference in hand, we next wanted to answer the question: how do these structural differences result in different turnover-limiting transition states?

Arene Structure Impact. In order to gain more insight into this divergent reactivity, we first explored the impact of electron density on the molecular system. Given the two structures (**6** and **8**), the difference in the systems is the replacement of three H atoms with three electronegative F atoms next to the carbonyl. To explore why the trifluoromethyl system has a decrease in $\Delta G_C^{\ddagger}$ and an increase in $\Delta G_{RC}^{\ddagger}$, we examined the impact of electron density on the aromatic ring adjacent to the carbonyl via a theoretical Hammett analysis. For this analysis, given the similar change in energy from the lowest energy conformer ($\mathbf{15a_{Me}}$, $\mathbf{15a_{CF3}}$) to the reactive conformer ($\mathbf{15b_{Me}}$, $\mathbf{15b_{CF3}}$) between both methyl and

https://doi.org/10.1021/acsomega.4c09880
ACS Omega 2025, 10, 10283−10293

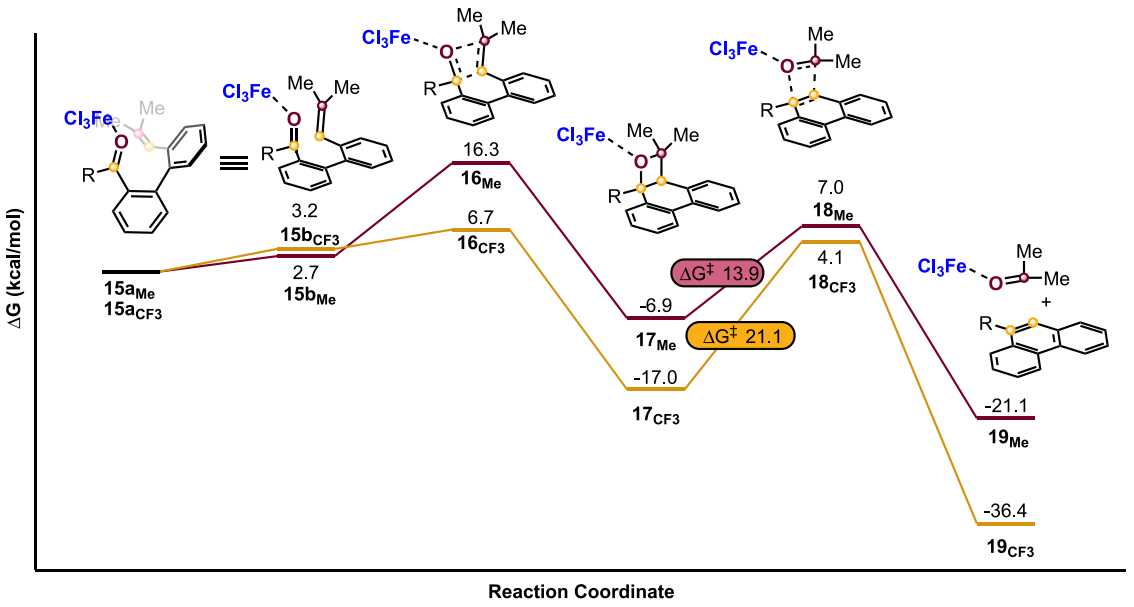

Figure 2. DFT-simulated reaction coordinates of the $FeCl_3$-catalyzed carbonyl−olefin metathesis of the methyl (Brown solid line) and trifluoromethyl (Yellow solid line) polyaromatic hydrocarbon systems. All energies were calculated on the revDSD-PBEP86-D4/def2-TZVPPD Toluene SMD level of theory. Free energies shown are in kcal/mol.

trifluoromethyl systems (Figure 2), the energies reported for all Hammett systems are relative to the reactive conformer.

To accomplish our theoretical Hammett analysis, we employed a range of aromatic functional groups on both the methyl and trifluoromethyl systems (Figure 3E). We chose to perform our analysis of these reaction paths by restricting the substitution to the meta and para positions about the aromatic ring relative to the carbonyl because of the potential for steric interference within the transition state structures of the ortho position. Applying the same level of theory used in Figure 2, we began with the cycloaddition of the methyl and trifluoromethyl systems (Figure 3A,B, Green solid circle). Examination of cycloaddition transition states of the methyl system displays a decrease in $\Delta G_C^{\ddagger}$ relative to the Hammett constant (Figure 3A, Green solid circle). Similar examination of the trifluoromethyl system displays an analogous negative correlation (Figure 3B, Green solid circle). These observations suggest an increase in positive charge around the carbonyl benefits the formation of the oxetane intermediate, lowering the barrier.

Turning our attention to the retro-cycloaddition for the two systems, we observe a positive correlation. For the methyl system, as the Hammett constant increases, $\Delta G_{RC}^{\ddagger}$ increases (Figure 3A, Brown solid circle). Similarly, the value of $\Delta G_{RC}^{\ddagger}$ for the trifluoromethyl system, though with a larger margin of error, increases with increasing Hammett constant (Figure 3B, Brown solid circle). These data are consistent with an increase in the barrier for the retro-cycloaddition from the oxetane intermediate as positive charge builds up.

Taken together, examination of both mechanistic steps of the reaction pathway shows a clear dependence on the inductive effects of the arene group. The cycloaddition becomes easier to accomplish as the electronegativity of the arene increases; whereas, the retro-cycloaddition becomes more difficult as the electronegativity of the arene grows. These twin observations suggest there may be a transition point at which the acid-mediated carbonyl−olefin metathesis reaction becomes an acid-mediated oxetane-forming process due to the buildup of positive charge in the system.

Because of this importance of charge, we next sought to examine how the buildup of positive charge at the carbonyl carbon (C1) is manifesting via NBO analysis. Using the same set of structures employed for $\Delta G_C^{\ddagger}$ and $\Delta G_{RC}^{\ddagger}$, we assessed the charges produced from natural population analysis, hereafter referred to as the NBO charge, at C1 relative to the Hammett constant. Beginning with the cycloadditions of the methyl system, we observe a negligible change in NBO charge relative to an increasing Hammett constant (Figure 3C, Green solid circle). With respect to the retro-cycloadditions of the methyl system, we again observe a negligible change in NBO charge relative to an increasing Hammett constant (Figure 3C, Brown solid circle). We observe an analogous trend in the trifluoromethyl system, albeit at a decreased overall charge for the retro-cycloaddition (Figure 3D, Brown solid circle). This lack of change suggests that, while there is an impact on the energies for the cycloaddition and retro-cycloaddition transition states relative to the Hammett constant, arene substitution inductive effects do not appear to be manifesting themselves as charge buildup on C1. Yet, when looking at the retro-cycloaddition charges, it is clear that there is a decrease in C1 charge for all substrates when going from the methyl system to the trifluoromethyl system (Figure 3C,D, Brown solid circle).

When we combine these analyses, we observe the following: (1) The $\Delta G_C^{\ddagger}$ for both systems decreases the same with increasing Hammett values. (2) All calculated $\Delta G_C^{\ddagger}$ values for the methyl system are larger than all values of the trifluoromethyl system. (3) The $\Delta G_{RC}^{\ddagger}$ for both systems increases at the same rate with increasing Hammett values. (4) All calculated $\Delta G_{RC}^{\ddagger}$ values for the methyl system are smaller than their trifluoromethyl system counterparts. (5) For each transition state, the NBO charge of C1 is approximately the same for all substrates in the methyl system and all substrates in the trifluoromethyl system. (6) For the retro-cycloaddition transition state, all calculated NBO charge values for the

https://doi.org/10.1021/acsomega.4c09880
ACS Omega 2025, 10, 10283−10293

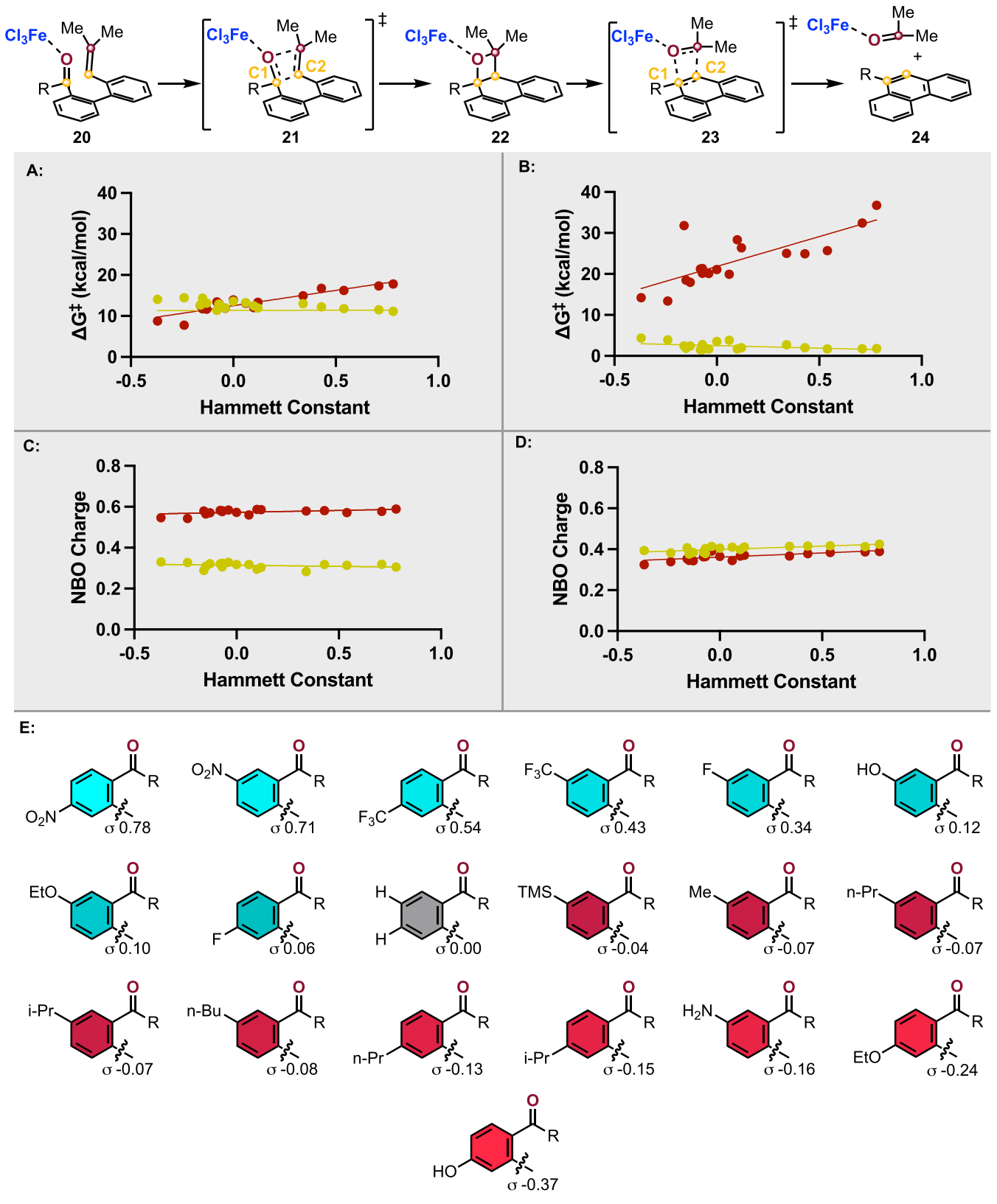

Figure 3. Theoretical Hammett analyses for the methyl (**A, C, R = Me**) and trifluoromethyl (**B, D, R = CF_3**) systems. Comparison of $\Delta G_C^{\ddagger}$ (Green solid circle) and $\Delta G_{RC}^{\ddagger}$ (Brown solid circle) for the methyl system (A), $\Delta G_C^{\ddagger}$ (Green solid circle) and $\Delta G_{RC}^{\ddagger}$ (Brown solid circle) for the trifluoromethyl system (B), C1 NBO Charge of the cycloaddition (Green solid circle) and retro-cycloaddition (Brown solid circle) for the methyl system (C), C1 NBO Charge of the cycloaddition (Green solid circle) and retro-cycloaddition (Brown solid circle) for the trifluoromethyl system (D) relative to the Hammett constant. Structure of each corresponding Hammett substituent (E). All free energies were calculated on the revDSD-PBEP86-D4/def2-TZVPPD Toluene SMD level of theory. Free energies shown are in kcal/mol.

https://doi.org/10.1021/acsomega.4c09880
ACS Omega 2025, 10, 10283−10293

methyl system are greater than all values of the trifluoromethyl system. Taken together, both systems generally display the same trends with respect to the employed Hammett constants. The repeated difference between both systems is with respect to the magnitude of those values. While the different functional groups are all impacting the reaction coordinate, the overriding difference between the behavior of both systems seems to be attributed to the replacement of the three H atoms at the α-position with three F atoms. To this end, we next explored how the F atoms impacted the mechanism.

Fluorination Impact. In order to gauge the influence F atoms have on the system, we performed the same reaction coordinate analysis as Figure 2, adding $-CH_2F$ and $-CHF_2$ systems (Figure 4). The sequential incorporation of F atoms

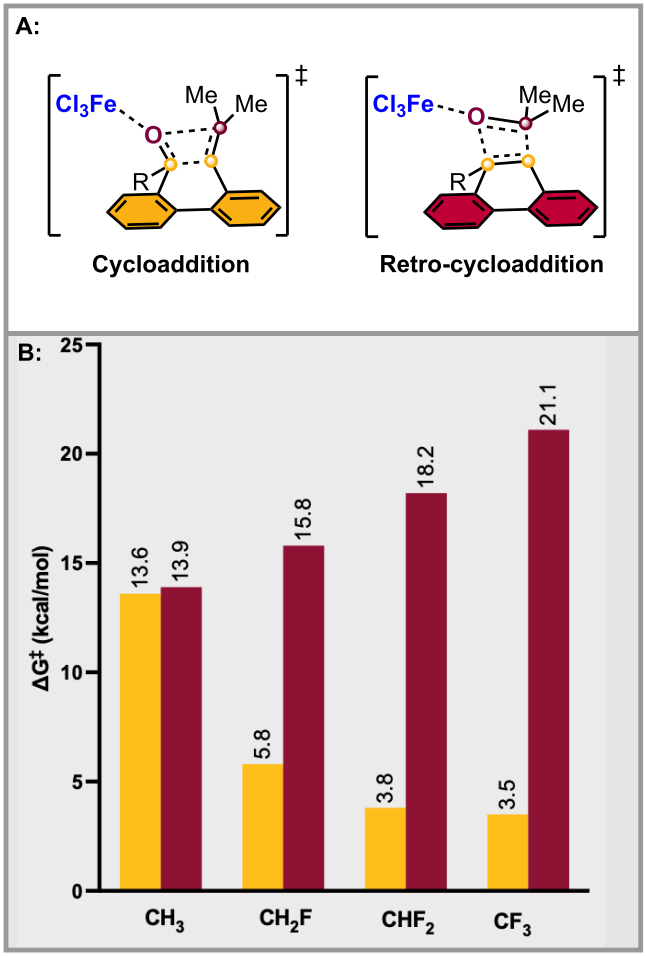

Figure 4. Transition state structures of the cycloaddition and the retro-cycloaddition steps (A). $\Delta G_C^{\ddagger}$ (gold) and $\Delta G_{RC}^{\ddagger}$ (maroon) for varying levels of fluorinated substrates (B). All free energies were calculated on the revDSD-PBEP86-D4/def2-TZVPPD Toluene SMD level of theory. Free energies shown are in kcal/mol.

adjacent to the carbonyl reduces $\Delta G_C^{\ddagger}$ with each additional fluorine, up to two (Figure 4B, gold). As we have discussed, the methyl system has a $\Delta G_C^{\ddagger}$ of 13.6 kcal/mol. The incorporation of the first F atom reduces $\Delta G_C^{\ddagger}$ to 5.8 kcal/mol, while the second and third fluorine reduces $\Delta G_C^{\ddagger}$ further to 3.8 and 3.5 kcal/mol, respectively. The overall trend is consistent with our observations that electron withdrawing groups in proximity to the carbonyl reduce the energetic barrier to oxetane formation.

Next, we explored the impact of F atom addition on $\Delta G_{RC}^{\ddagger}$ (Figure 4B, maroon). As we have discussed, the methyl system has a $\Delta G_{RC}^{\ddagger}$ of 13.9 kcal/mol. The incorporation of the first fluorine increases $\Delta G_{RC}^{\ddagger}$ to 15.8 kcal/mol. The second F atom increases $\Delta G_{RC}^{\ddagger}$ further to 18.2 kcal/mol, with the third fluorine increasing $\Delta G_{RC}^{\ddagger}$ further to 21.1 kcal/mol.

This trend is consistent with our observations that electron withdrawing groups in proximity to the carbonyl increase the barrier to metathesis product formation.

In our proposed mechanism for carbonyl−olefin metathesis, the asynchronous [2 + 2]-cycloaddition occurs via "fast" formation of the C1−C2 bond and "slow" formation of the C3−O bond (Figure 5).[17] Conversely, the retro-[2 + 2]-cycloaddition likely occurs via "fast" cleavage of the C1−O bond and "slow" cleavage of the C2−C3 bond. We have already shown that adjustments to electron density via arene substitution around C1 have no impact on its NBO charge (Figure 3); yet, we believed we could paint a more complete picture by further tracking the C1 NBO charge as well as atomic distances of each state across the reaction coordinate for each degree of fluorination (Figure 5). Beginning with the reactive conformer of the activated starting material, we observe through-space distances between C1 and C2 with small variations across the systems: 2.93 Å for CH_3, 2.75 Å for CH_2F, 2.90 Å for CHF_2, and 2.75 Å for CF_3 (Figure 5A). While the CF_3 system has a shorter distance between C1 and C2 than in the CH_3 system, a clear trend related to an increasing number of F atoms does not present itself. There is, however, a negative relationship of C1 NBO charge with an increasing number of F atoms. The C1 NBO charges we observe are 0.71, 0.66, 0.63, and 0.62 with increasing fluorination. The set displays a total decrease in C1 NBO charge of 0.09.

We then examined the [2 + 2]-cycloaddition transition state (Figure 5B). Unsurprisingly, the C1−C2 distances for the set are substantially shorter for the transition state. However, again, we see that all four transition states display small variations in atom distances, with the C1−C2 distance of the CF_3 system being the longest of the set. We observe a C1−C2 distance of 1.59, 1.58, 1.89, and 1.91 Å with increasing fluorination. Interestingly, we observe a slight decrease in C1 NBO Charge across the set until a significant increase when three F atoms are present: 0.32, 0.27, 0.22, and 0.41 with increasing fluorination.

In order to explore the impact on the oxetane conformer and the retro-[2 + 2]-cycloaddition transition state, we turned our attention to the C1−O bond. Examination of the oxetane conformer displays no variation in geometry across the set (Figure 5C). We observe a bond distance of 1.56, 1.53, 1.51, and 1.50 Å with increasing fluorines. However, we do observe a decrease in NBO charge at C1 with an increasing number of F atoms: 0.33, 0.26, 0.23, and 0.20. These structures display a total decrease of 0.12 across the set. As with the oxetane, we observe no variation in the geometry of the transition state across the set for the retro-[2 + 2]-cycloaddition, with a C1−O bond distance of 2.28, 2.29, 2.31, and 2.33 Å with increasing F atoms (Figure 5D). Conversely, we observe the largest change in C1 NBO charge across the set. We observe charges of 0.57, 0.49, 0.42, and 0.37 with an increase in fluorination: an overall decrease of 0.20, representing a 35% reduction in C1 NBO charge. This decrease in C1 NBO charge for the retro-[2 + 2]-cycloaddition transition state stands in contrast to our Hammett data (Figures 3C,D). As more electron density is

https://doi.org/10.1021/acsomega.4c09880
ACS Omega 2025, 10, 10283−10293

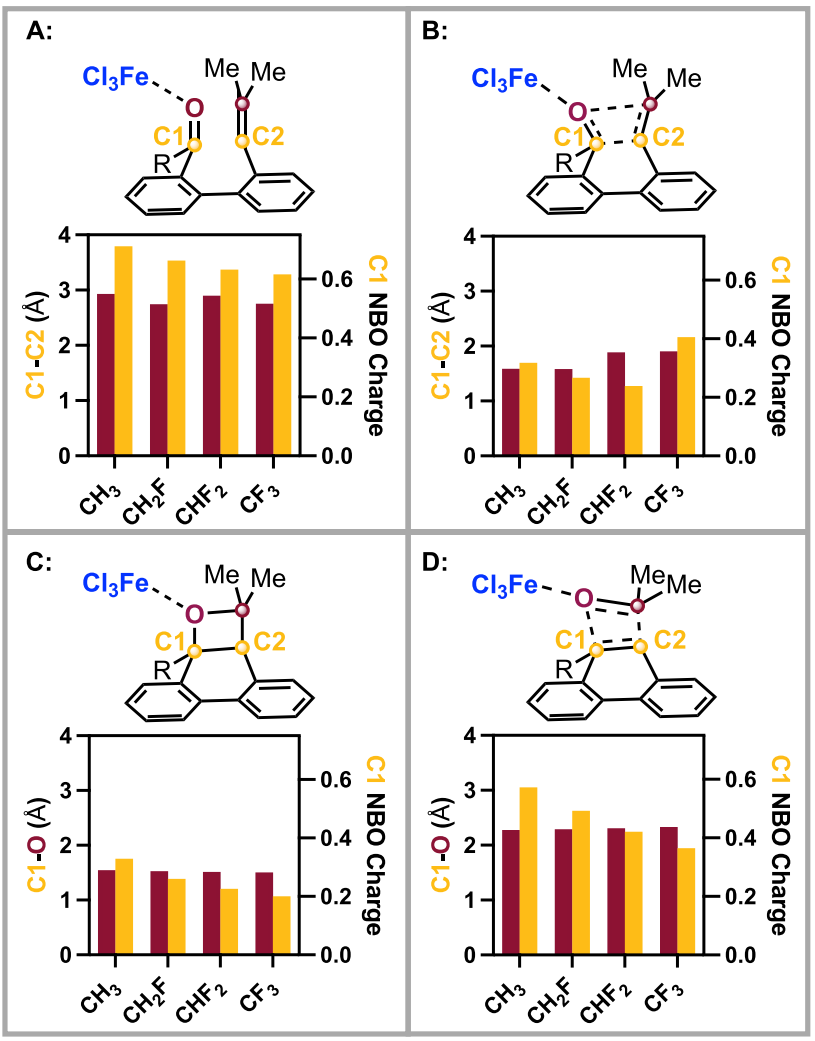

Figure 5. Distances between C1 & C2 (maroon) and C1 NBO charges (gold) for reactive starting material conformer (A) and the cycloaddition transition state (B). Distances between C1 & O (maroon) and C1 NBO charges (gold) for reactive oxetane conformer (C) and the retro-cycloaddition transition state (D). NBO charges were derived from single-point energy calculations using the wB97X-D3/def2-TZVP Toluene SMD level of theory.

withdrawn from the aromatic ring adjacent to C1, we observe a negligible change in NBO charge at C1 in the transition state, which we do not observe with increased attachment of F atoms at the carbon α to C1. This differential effect suggests that replacement of H atoms with F atoms in these systems is producing a change beyond simple inductive effects.

Orbital Analysis. Due to the fact that we are examining the overall energetic impact of the replacement of H atoms with F atoms, as well as the specific impact on charge, we wondered how the electrons in the C−H and C−F σ-bonds impacted the charge at C1. First reported by Baker and Nathan,[23] hyperconjugation, as named by Mulliken, Rieke, and Brown,[24] is the mixing of σ-bonds with a network of π-bonds.[25] As typically presented in sophomore organic chemistry, C−H and C−C σ-bonds can also interact with unfilled or partially filled π- or p-orbitals. Alternatively, C−F bonds can participate in negative hyperconjugation, or the mixing of the σ^* antibonding orbital with filled π- or p-orbitals. To examine these stereoelectronic effects, we applied a second order perturbation theory analysis of the Fock matrix in NBO basis. This method assesses the energy stabilizing effects of natural localized molecular orbital (NLMO) electron density donation to unoccupied NLMOs.[26]

Because both systems display competent ability to form the oxetane intermediate via [2 + 2]-cycloaddition, we directed our focus to the substrate-dependent retro-[2 + 2]-cycloaddition. During the retro-cycloaddition step, there is a partially vacant C1 p-orbital as the C1−O bond breaks (Figure 6A). For the methyl system, we observe significant overlap of the C_α−H_a and C_α−H_b σ bonds with the C1 p-orbital (Figure 6B). These interactions contribute stabilization energies of 13.7 kcal/mol via the C_α−H_a σ-bond, 3.3 kcal/mol via the C_α−H_b σ bond, and a much smaller 0.7 kcal/mol via the C_α−H_c σ bond. For the CH_2F system, we again observe significant overlap of the C_α−H_a and C_α−H_b σ bonds with the C1 p-orbital (Figure 6C,D). In this most stable conformer, the C_α−F σ bond is almost orthogonal to the p-orbital at C1, providing a stabilization 0.4 kcal/mol. The two C−H σ-bond interactions contribute stabilization energies of 10.4 kcal/mol via the C_α−H_a σ-bond and 5.5 kcal/mol via the C_α−H_b σ bond, representing a more distributed contribution by these two σ-bonds.

https://doi.org/10.1021/acsomega.4c09880
ACS Omega 2025, 10, 10283−10293

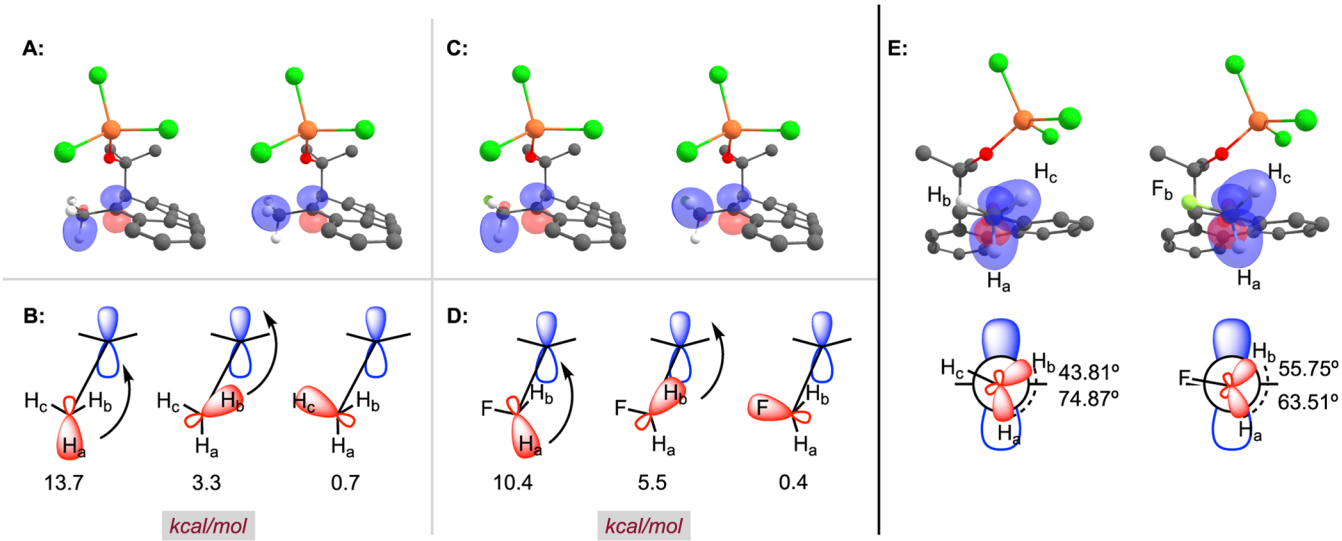

Figure 6. 3D representation of the C−H σ bond overlap for the CH_3 system (A). Sawhorse projection of the stabilizing orbital contributions to the C1 p-orbital of the breaking transient C−O bond for the CH_3 system (B). 3D representation of the C−H σ bond overlap for the CH_2F system (C). Sawhorse projection of the stabilizing orbital contributions to the C1 p-orbital of the breaking transient C−O bond for the CH_2F system (D). 3D structures and Newman projections of the orbital overlap for the CH_3 and CH_2F systems (E). NBO charges were derived from single-point energy calculations using the wB97X-D3/def2-TZVP Toluene SMD level of theory.

Closer examination of the geometries of the most stable methyl and fluoromethyl conformers yields more insight into these stereoelectronic effects. The Newman projection of the methyl derivative along the C_α−C1 bond displays a 74.87° dihedral angle from H_a to the "arene plane" and 43.81° from H_b. Meanwhile, for the CH_2F derivative, the angle decreases to 63.51° for H_a, increasing H_b to 55.75°. This shift results in overlap of both the C−H_a and C−H_b σ-bonds with the empty p-orbital.

Increasing the number of α-carbon fluorine atoms to two requires a different mechanism of charge stabilization from hyperconjugation. The three-dimensional (3D) representation of the NBO orbitals displays a shift of the vacant p-orbital onto the bridging carbon of the aromatic ring adjacent to C1 (Figure 7A). Due to this shift in orbital vacancy and the observed decrease in charge at C1, we wondered how the number of F atoms impacted the NBO charge of the aromatic rings (Figure 7C). Compared to the decrease in C1 NBO charge relative to the number of F atoms, there is a simultaneous increase in arene NBO charge. The first F atom yields a nominal increase in NBO charge across the arenes of 0.04. However, the second F atom yields a larger increase in charge of 0.09. Arriving at the trifluoromethyl, we again observe a nominal increase in charge of 0.03. Overall, these changes with an increasing number of F atoms result in an 84% increase in charge distributed across the aromatic rings. This 84% increase in the rings is concomitant with a 35% decrease in charge at C1. Notably, the largest increase in charge is associated with the transition of the vacant p-orbital into the aromatic carbons.

To examine the fundamental aspects of these observations from our model, we explored a simpler system: the *tert*-butyl carbocation. Rasul, Chen, Prakash, and Olah exhaustively characterized the structure/activity of this important intermediate, and we applied their geometry as a starting point.[27] Because our carbonyl−olefin metathesis model explores the impact of the degree of fluorination on one carbon adjacent to an unoccupied p-orbital, we varied fluorination at only one of the α-carbons. When there are no fluorine groups present, all CH_3 groups assume a C_s geometry in which there is one C−H σ-bond at each α-carbon parallel with the unoccupied p-orbital, as was previously reported (Figure 8A).[27] In this conformation, hyperconjugation at each methyl is localized primarily within a single C−H bond. When one fluorine is present, the fluorinated group rotates to have the fluorine on the same plane as the sp^2 center, and the two remaining C−H σ-bonds both interact with the empty p-orbital (Figure 8B). This fluorine-induced rotation results in hyperconjugation of the CH_2F group being distributed across both C−H bonds. When two fluorine atoms are present, the remaining C−H σ-bond is again parallel with the empty p-orbital (Figure 8C). The other methyl groups assume a symmetrical conformation, yielding a C_s geometry in which each has two C−H σ bonds which overlap with the unoccupied p-orbital. When a CF_3 group is present, the same conformation as the CHF_2 is adopted, again yielding a C_s geometry. However, there is a relatively small amount of overlap from the fluorine lone-pair with the unoccupied p-orbital.

When both models are examined in parallel, we observe that hyperconjugation in the methyl system is most analogous to the *tert*-butyl cation. The fluoromethyl system is most analogous to the CH_2F-substituted cation. So too are the difluoro and trifluoro systems most analogous with the difluoro and trifluoro cations, respectively. These analogous data suggest that in fluorinated carbocations, conformers that maximize C−H σ overlap with the vacant p-orbital are preferred.

Overall Mechanistic Proposal. Our quantum chemical simulations predict the following: (1) Examination of the reaction coordinate for the $FeCl_3$-catalyzed reactions of **6** and **8** reveals that the incorporation of F atoms decreases $\Delta G_C^{\ddagger}$. (2) Conversely, the inclusion of F atoms in **8** increases $\Delta G_{RC}^{\ddagger}$. (3) As the Hammett constants of aromatic substituents increase for both systems, there is a decrease in $\Delta G_C^{\ddagger}$. (4) Simultaneously, increasing σ results in an increase in $\Delta G_{RC}^{\ddagger}$. (5) With the exception of a single substituent, $\Delta G_{RC}^{\ddagger}$ is greater

https://doi.org/10.1021/acsomega.4c09880
ACS Omega 2025, 10, 10283−10293

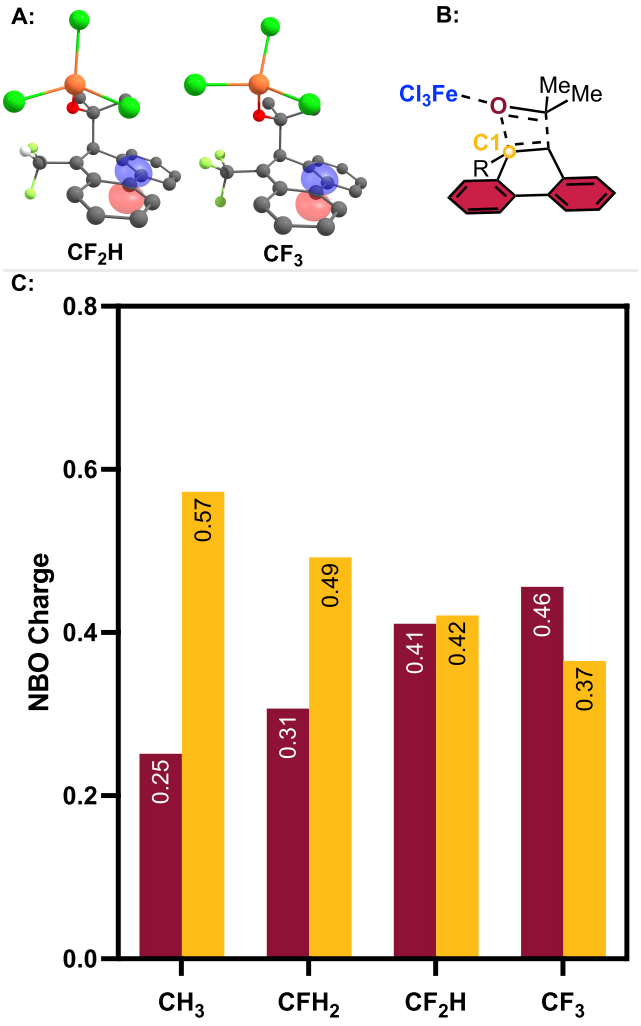

Figure 7. 3D representations of charge delocalization into the aromatic ring for CF_2H and CF_3 systems (A). Atoms selected for NBO analysis (B). C1 NBO charge (gold) and the sum of the H and C NBO charges of the aromatic rings (maroon) relative to the number of α-carbon fluorine atoms (C). NBO charges were derived from single-point energy calculations using the wB97X-D3/def2-TZVP Toluene SMD level of theory.

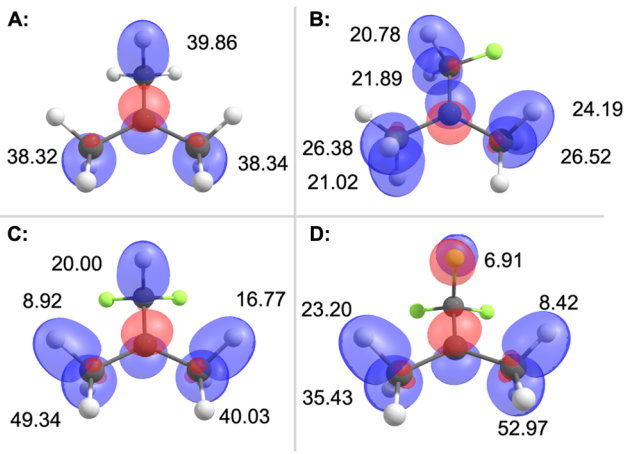

Figure 8. Orbital overlap for various carbocations: 2-methylpropan-2-ylium ion (A), 1-fluoro-2-methylpropan-2-ylium ion (B), 1,1-difluoro-2-methylpropan-2-ylium ion (C), and 1,1,1-trifluoro-2-methylpropan-2-ylium ion (D). All numerical values are in kcal/mol. NBO charges were derived from single-point energy calculations using the wB97X-D3/def2-TZVP Toluene SMD level of theory.

than $\Delta G_C^{\ddagger}$ for all CF_3-bearing molecules. (6) For both systems, the NBO charge at C1 is essentially constant for all substituents in both transition states. (7) In the trifluoromethyl system, the retro-cycloaddition charge at C1 is approximately 0.2 less than the methyl system for all aromatic substituents. (8) Increasing the number of F atoms α to the carbonyl up to two decreases $\Delta G_C^{\ddagger}$. (9) $\Delta G_{RC}^{\ddagger}$ increases as H atoms are substituted with F atoms. (10) Increasing the number of F atoms α to the carbonyl has an inconsistent impact on the charge at C1 in the cycloaddition. (11) In the retro-cycloaddition, the charge at C1 decreases with increasing number of F atoms. (12) In the retro-cycloaddition, the positive charge is localized to C1 for the CH_3 and CH_2F motifs and is supported by hyperconjugation. (13) The positive charge of the retro-cycloaddition is delocalized into the aromatic rings for the CHF_2 and CF_3 motifs.

Taken together, these data suggest that the methyl system proceeds via turnover-limiting [2 + 2]-cycloaddition, consistent with our kinetic observations.[17] Similarly, the CF_3 system also proceeds via turnover-limiting [2 + 2]-cycloaddition; however, reactivity terminates at the oxetane intermediate due to an insurmountable $\Delta G_{RC}^{\ddagger}$. This increased barrier may be a factor in the application of heat the Schindler group employed to isolate a trifluoromethylphenanthrene from a styrenyl olefin system;[16c] whereas, there is no matching observation for the prenyl olefin system we have examined. Further, the increased $\Delta G_{RC}^{\ddagger}$ is associated with a decrease in the hyperconjugation ability of the σ bonds on the carbon α to the carbonyl. Complete metathesis reactivity appears to be associated with charge that is able to be localized at the carbonyl carbon for the duration of the cycle. Delocalization of this charge is associated with an inability to complete the terminal retro-[2 + 2]-cycloaddition. With these observations in hand, it is necessary to enumerate other predictions that result from our model.

The substrate library we employed in our theoretical Hammett analysis leads to a number of predictions of possible synthetic targets. In their original work, Schindler and co-workers widely varied the substituents on the olefin-bearing ring, showing that groups ranging from electron-withdrawing to electron-donating resulted in successful carbonyl−olefin metathesis (Figure 9A).[16c] Our model suggests that, if the $\Delta G_{RC}^{\ddagger}$ is high enough, the metathesis reaction will stop at the oxetane intermediate. For the theoretical Hammett analysis, the majority of the trifluoromethyl derivatives have a high $\Delta G_{RC}^{\ddagger}$. Therefore, our model predicts that these trifluoromethyl derivatives could potentially produce a library of oxetane forming substrates (Figure 9B).[28] Conversely, the $\Delta G_{RC}^{\ddagger}$ of the methyl derivatives are relatively lower. For that reason, our model predicts that these methyl derivatives could potentially produce a library of metathesis substrates (Figure 9A). The calculated monofluoro and difluoro derivative transition state energies and NBO charges give us insight into their possible empirical outcomes. The $\Delta G_{RC}^{\ddagger}$ for the monofluoro derivative is closer in energy to that of the methyl derivative than it is the trifluoro derivative. Conversely, the difluoro derivative's $\Delta G_{RC}^{\ddagger}$ is closer to that of the trifluoromethyl derivative than it is to the methyl derivative. Comparison of the NBO charges provides further differentiation. For the methyl and monofluoro derivatives, the lone

https://doi.org/10.1021/acsomega.4c09880
ACS Omega 2025, 10, 10283−10293

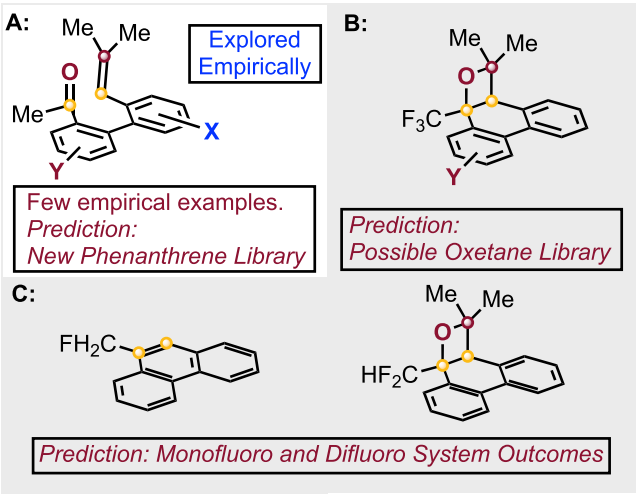

Figure 9. Experimentally explored olefin ring substitution (**X**) and potential phenanthrene library as produced through substitution at the carbonyl aromatic ring (**Y**) (A). Potential oxetane library as produced through substitution at the carbonyl aromatic ring (B). Predicted outcomes for fluoromethyl and difluoromethyl systems (C).

valence NBO lies on C1. For the difluoro and trifluoro derivatives, the lone valence moves into the aromatic ring. Based on these data, our model predicts that the monofluoro derivative should produce the phenanthrene product, while the difluoro derivative should stop at the oxetane (Figure 9C). Importantly, we have only observed either exclusive metathesis reactivity or exclusive oxetane reactivity. The predictions our model makes for the changes in transition state energies suggest that there is likely a point of transition where the olefin-forming process becomes an oxetane-forming process, and this transition may include product mixtures. Starting with the methyl system, we can expect the fewest candidates to result in oxetane, with the number of oxetane candidates increasing as the number of α-F atoms increases.

In addition to offering a scope of predictions, it is critical to determine the explanatory power of our model. In other words, does the scope of our model extend beyond aromatic ketones? As we described above, Schindler and co-workers isolated an oxetane from a completely different substrate system: **11** (Figure 1).[16e] A notable feature of this system is that the Lewis acidic $FeCl_3$ behaves as a dimer in the catalytic cycle. Because our model is based on the impact of substrate structure, this deviation in catalyst behavior should not impact its predictions, if our model is broadly applicable for $FeCl_3$-catalyzed carbonyl−olefin metathesis. According to our model, we can hypothesize that we should see a more positive value for $\Delta G_{RC}^{\ddagger}$ than for $\Delta G_{C}^{\ddagger}$ in this system, with the $\Delta G_{RC}^{\ddagger}$ being sufficiently large. To test this hypothesis, we examined the reaction coordinate for the $FeCl_3$- catalyzed conversion of **10** to **11** (Figure 10). For this system, we see that a [2 + 2]-cycloaddition results in a $\Delta G_{C}^{\ddagger}$ of 9.4 kcal/mol. Further, a retro-[2 + 2]-cycloaddition requires a $\Delta G_{RC}^{\ddagger}$ of 20.6 kcal/mol, far larger than $\Delta G_{C}^{\ddagger}$.

CONCLUSIONS

We have developed a model that shows how substrate structure impacts the trajectory of the carbonyl−olefin metathesis reaction. Through a theoretical Hammett analysis, we have shown that electron-withdrawing aromatic substituents decrease cycloaddition transition state energies and increase retro-cycloaddition energies. We observe hyperconjugative effects from α-carbon protons that aid in stabilizing the buildup of positive charge during the retro-cycloaddition. Furthermore, we see that as the amount of hyperconjugative donation decreases, positive charge increases across the aromatic ring. Taken together, our model suggests that a major factor in oxetane isolation is the substrate's inability to stabilize the retro-cycloaddition transition state partial charge.

By examining the substrate impact on the $FeCl_3$-catalyzed carbonyl−olefin metathesis reaction, we are able to propose an explanation for the observed aromatic oxetane **9** as reported by Schindler and co-workers. Further, we were able to apply this model to explain the isolation of oxetane **11** in the aliphatic system by Schindler and co-workers.[16e] Additionally, we predict a point of transition where the olefin-forming process becomes an oxetane-forming process, leading to potential phenanthrene and oxetane forming substrate libraries. We are currently investigating how fluorination impacts the energetics of aliphatic substrates to see if the inclusion of these atoms can be expanded beyond aromatic systems. We have also begun the synthesis of several substrate platforms to test the predictions

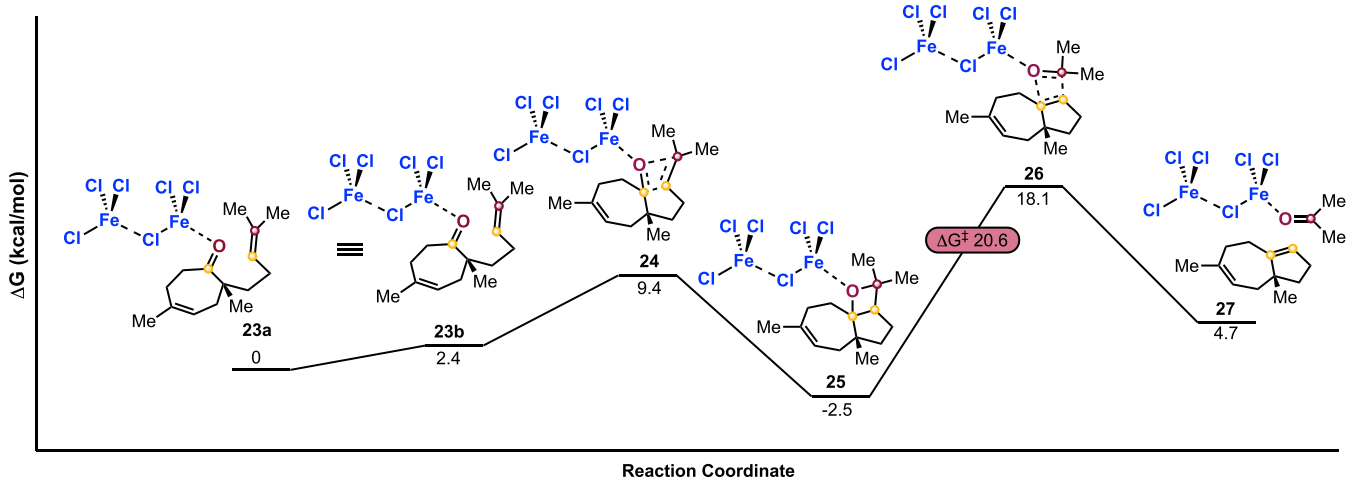

Figure 10. DFT-calculated reaction coordinate of the carbonyl−olefin metathesis of **10.** All free energies were calculated on the revDSD-PBEP86-D4/def2-TZVPPD 1,2-DCE SMD level of theory. Free energies shown are in kcal/mol.

https://doi.org/10.1021/acsomega.4c09880
ACS Omega 2025, 10, 10283−10293

which result from our model. The intention is to systematically develop a model of substrate behavior. We will report these results in due course.

METHODS

For a comparative analysis of different computational methods, including various density functionals and basis sets, which were used to calculate the energies of the reaction coordinate shown in Figure 2, see Supporting Information, Section 1. Conformer searches were performed using Spartan '20 via a conformer distribution calculation using molecular mechanics (MMFF) with a 40 kJ/mol pruning window from the lowest energy conformer and a maximum of 500 conformers. Each conformer was then optimized using the B97-D density functional and employing the double-ζ, 6-31G* basis set along with a CPCM solvent model (Toluene or 1,2-DCE), followed by a revDSD-PBEP86-D4/def2-TZVPPD SMD solvent model (Toluene or 1,2-DCE) single point calculation (Supporting Information, Section 2). For an examination of a possible stepwise pathway as an alternative, see Supporting Information, Section 3. The results described agree with the short-lived intermediates predicted previously.[17] For our application of the energetic span model, see Supporting Information, Section 4. We assessed charges using an NBO package that transforms the canonical delocalized MO's into localized, Lewis-like orbitals. The energetic importance of delocalization of "filled" orbitals to "empty" orbitals is calculated through second order perturbation theory (Supporting Information, Section 5).

ASSOCIATED CONTENT

Supporting Information

The Supporting Information is available free of charge at https://pubs.acs.org/doi/10.1021/acsomega.4c09880.

> The Supporting Information is available free of charge on the ACS Publications Web site. Computational details for optimized structures, free energies, NBO charges, and orbitals (PDF)

AUTHOR INFORMATION

Corresponding Author

James J. Devery, III − *Department of Chemistry & Biochemistry, Loyola University Chicago, Chicago, Illinois 60660, United States;* orcid.org/0000-0003-3124-465X; Email: jdevery@luc.edu

Author

Cory W. Schneider − *Department of Chemistry & Biochemistry, Loyola University Chicago, Chicago, Illinois 60660, United States*

Complete contact information is available at: https://pubs.acs.org/10.1021/acsomega.4c09880

Notes

The authors declare no competing financial interest.

ACKNOWLEDGMENTS

C.W.S. and J.J.D. thank the NIH under R15GM128126 and Loyola University Chicago for support.

REFERENCES

(1) (a) Albright, H.; Davis, A. J.; Gomez-Lopez, J. L.; Vonesh, H. L.; Quach, P. K.; Lambert, T. H.; Schindler, C. S. Carbonyl−Olefin Metathesis. *Chem. Rev.* **2021**, *121* (15), 9359−9406. (b) Becker, M. R.; Watson, R. B.; Schindler, C. S. Beyond olefins: new metathesis directions for synthesis. *Chem. Soc. Rev.* **2018**, *47* (21), 7867−7881. (c) Ludwig, J. R.; Schindler, C. S. Lewis Acid Catalyzed Carbonyl-Olefin Metathesis. *Synlett* **2017**, *28* (13), 1501−1509. (d) Ravindar, L.; Lekkala, R.; Rakesh, K. P.; Asiri, A. M.; Marwani, H. M.; Qin, H.-L. Carbonyl−olefin metathesis: a key review. *Org. Chem. Front.* **2018**, *5* (8), 1381−1391.

(2) (a) Stille, J. R.; Grubbs, R. H. Synthesis of (.+-.)-.DELTA.9,12-capnellene using titanium reagents. *J. Am. Chem. Soc.* **1986**, *108* (4), 855−856. (b) Stille, J. R.; Santarsiero, B. D.; Grubbs, R. H. Rearrangement of bicyclo[2.2.1]heptane ring systems by titanocene alkylidene complexes to bicyclo[3.2.0]heptane enol ethers. Total synthesis of (.+-.)-.DELTA.9(12)-capnellene. *J. Org. Chem.* **1990**, *55* (3), 843−862. (c) Nicolaou, K. C.; Postema, M. H. D.; Claiborne, C. F. Olefin Metathesis in Cyclic Ether Formation. Direct Conversion of Olefinic Esters to Cyclic Enol Ethers with Tebbe-Type Reagents. *J. Am. Chem. Soc.* **1996**, *118* (6), 1565−1566.

(3) (a) Griffith, A. K.; Vanos, C. M.; Lambert, T. H. Organocatalytic carbonyl-olefin metathesis. *J. Am. Chem. Soc.* **2012**, *134* (45), 18581−18584. (b) Hong, X.; Liang, Y.; Griffith, A. K.; Lambert, T. H.; Houk, K. N. Distortion-Accelerated Cycloadditions and Strain-Release-Promoted Cycloreversions in the Organocatalytic Carbonyl-Olefin Metathesis. *Chem. Sci.* **2014**, *5* (2), 471−475. (c) Zhang, Y.; Jermaks, J.; MacMillan, S. N.; Lambert, T. H. Synthesis of 2H-Chromenes via Hydrazine-Catalyzed Ring-Closing Carbonyl-Olefin Metathesis. *ACS Catal.* **2019**, *9* (10), 9259−9264. (d) Lambert, T. H. Development of a Hydrazine-Catalyzed Carbonyl-Olefin Metathesis Reaction. *Synlett* **2019**, *30* (17), 1954−1965. (e) Jermaks, J.; Quach, P. K.; Seibel, Z. M.; Pomarole, J.; Lambert, T. H. Ring-opening carbonyl-olefin metathesis of norbornenes. *Chem. Sci.* **2020**, *11* (30), 7884−7895. (f) Zhang, Y.; Sim, J. H.; MacMillan, S. N.; Lambert, T. H. Synthesis of 1,2-Dihydroquinolines via Hydrazine-Catalyzed Ring-Closing Carbonyl-Olefin Metathesis. *Org. Lett.* **2020**, *22* (15), 6026−6030. (g) Holl, M. G.; Lambert, T. H. Ring-Opening Carbonyl-Olefin Metathesis of Cyclobutenes. *ACS Catal.* **2022**, *12* (9), 4813−4817. (h) Cho, E. K.; Quach, P. K.; Zhang, Y.; Sim, J. H.; Lambert, T. H. Polycyclic heteroaromatics via hydrazine-catalyzed ring-closing carbonyl-olefin metathesis. *Chem. Sci.* **2022**, *13* (8), 2418−2422.

(4) Pitzer, L.; Sandfort, F.; Strieth-Kalthoff, F.; Glorius, F. Carbonyl-Olefin Cross-Metathesis Through a Visible-Light-Induced 1,3-Diol Formation and Fragmentation Sequence. *Angew. Chem., Int. Ed.* **2018**, *57* (49), 16219−16223.

(5) Rivero-Crespo, M. N.; Tejeda-Serrano, M.; Pérez-Sánchez, H.; Cerón-Carrasco, J. P.; Leyva-Pérez, A. Intermolecular Carbonyl−olefin Metathesis with Vinyl Ethers Catalyzed by Homogeneous and Solid Acids in Flow. *Angew. Chem.* **2020**, *132* (10), 3874−3877.

(6) Scharf, D.; Korte, F. Photosensibilisierte cyclodimerisierung von norbornen. *Tetrahedron Lett.* **1963**, *4* (13), 821−823.

(7) van Schaik, H. P.; Vijn, R. J.; Bickelhaupt, F. Acid-Catalyzed Olefination of Benzaldehyde. *Angew. Chem., Int. Ed. Engl.* **1994**, *33* (15−16), 1611−1612.

(8) (a) Bah, J.; Franzén, J. Direct Organocatalytic Oxo-Metathesis, atrans-Selective Carbocation-Catalyzed Olefination of Aldehydes. *Eur. J. Org. Chem.* **2015**, *2015* (8), 1834−1839. (b) Ni, S.; Franzén, J. Carbocation catalysed ring closing aldehyde-olefin metathesis. *Chem. Commun.* **2018**, *54* (92), 12982−12985.

(9) (a) Catti, L.; Tiefenbacher, K. Brønsted Acid-Catalyzed Carbonyl-Olefin Metathesis Inside a Self-Assembled Supramolecular Host. *Angew. Chem., Int. Ed.* **2018**, *57* (44), 14589−14592. (b) Huck, F.; Catti, L.; Reber, G. L.; Tiefenbacher, K. Expanding the Protecting Group Scope for the Carbonyl Olefin Metathesis Approach to 2,5-Dihydropyrroles. *J. Org. Chem.* **2022**, *87* (1), 419−428.

(10) Tran, U. P. N.; Oss, G.; Pace, D. P.; Ho, J.; Nguyen, T. V. Tropylium-promoted carbonyl-olefin metathesis reactions. *Chem. Sci.* **2018**, *9* (23), 5145−5151.

(11) Tran, U. P. N.; Oss, G.; Breugst, M.; Detmar, E.; Pace, D. P.; Liyanto, K.; Nguyen, T. V. Carbonyl−Olefin Metathesis Catalyzed by Molecular Iodine. *ACS Catal.* **2019**, *9* (2), 912−919.

(12) Anh To, T.; Pei, C.; Koenigs, R. M.; Vinh Nguyen, T. Hydrogen Bonding Networks Enable Brønsted Acid-Catalyzed Carbonyl-Olefin Metathesis. *Angew. Chem., Int. Ed.* **2022**, *61* (13), No. e202117366.
(13) Djurovic, A.; Vayer, M.; Li, Z.; Guillot, R.; Baltaze, J.-P.; Gandon, V.; Bour, C. Synthesis of Medium-Sized Carbocycles by Gallium-Catalyzed Tandem Carbonyl−Olefin Metathesis/Transfer Hydrogenation. *Org. Lett.* **2019**, *21* (19), 8132−8137.
(14) Davis, A. J.; Watson, R. B.; Nasrallah, D. J.; Gomez-Lopez, J. L.; Schindler, C. S. Superelectrophilic Aluminium(III)−Ion Pairs Promote a Distinct Reaction Path for Carbonyl−Olefin Ring-Closing Metathesis. *Nat. Catal.* **2020**, *3* (10), 787−796.
(15) Wang, R.; Chen, Y.; Shu, M.; Zhao, W.; Tao, M.; Du, C.; Fu, X.; Li, A.; Lin, Z. $AuCl_3$-Catalyzed Ring-Closing Carbonyl-Olefin Metathesis. *Chem. - Eur. J.* **2020**, *26* (9), 1941−1946.
(16) (a) Ludwig, J. R.; Zimmerman, P. M.; Gianino, J. B.; Schindler, C. S. Iron(III)-catalysed carbonyl-olefin metathesis. *Nature* **2016**, *533* (7603), 374−379. (b) Ma, L.; Li, W.; Xi, H.; Bai, X.; Ma, E.; Yan, X.; Li, Z. $FeCl_3$-Catalyzed Ring-Closing Carbonyl-Olefin Metathesis. *Angew. Chem., Int. Ed.* **2016**, *55* (35), 10410−10413. (c) McAtee, C. C.; Riehl, P. S.; Schindler, C. S. Polycyclic Aromatic Hydrocarbons Via Iron(III)-Catalyzed Carbonyl−Olefin Metathesis. *J. Am. Chem. Soc.* **2017**, *139* (8), 2960−2963. (d) Groso, E. J.; Golonka, A. N.; Harding, R. A.; Alexander, B. W.; Sodano, T. M.; Schindler, C. S. 3-Aryl-2, 5-Dihydropyrroles via Catalytic Carbonyl-Olefin Metathesis. *ACS Catal.* **2018**, *8* (3), 2006−2011. (e) Albright, H.; Riehl, P. S.; McAtee, C. C.; Reid, J. P.; Ludwig, J. R.; Karp, L. A.; Zimmerman, P. M.; Sigman, M. S.; Schindler, C. S. Catalytic Carbonyl-Olefin Metathesis of Aliphatic Ketones: Iron(III) Homo-Dimers as Lewis Acidic Superelectrophiles. *J. Am. Chem. Soc.* **2019**, *141* (4), 1690−1700. (f) Rykaczewski, K. A.; Groso, E. J.; Vonesh, H. L.; Gaviria, M. A.; Richardson, A. D.; Zehnder, T. E.; Schindler, C. S. Tetrahydropyridines via $FeCl_3$-Catalyzed Carbonyl-Olefin Metathesis. *Org. Lett.* **2020**, *22* (7), 2844−2848. (g) Ludwig, J. R.; Watson, R. B.; Nasrallah, D. J.; Gianino, J. B.; Zimmerman, P. M.; Wiscons, R. A.; Schindler, C. S. Interrupted carbonyl-olefin metathesis via oxygen atom transfer. *Science* **2018**, *361* (6409), 1363−1369. (h) Riehl, P. S.; Nasrallah, D. J.; Schindler, C. S. Catalytic, transannular carbonyl-olefin metathesis reactions. *Chem. Sci.* **2019**, *10* (44), 10267−10274. (i) Davis, A. J.; Watson, R. B.; Nasrallah, D. J.; Gomez-Lopez, J. L.; Schindler, C. S. Superelectrophilic aluminium(III)−ion pairs promote a distinct reaction path for carbonyl−olefin ring-closing metathesis. *Nat. Catal.* **2020**, *3* (10), 787−796.
(17) Ludwig, J. R.; Phan, S.; McAtee, C. C.; Zimmerman, P. M.; Devery, J. J.; Schindler, C. S. Mechanistic Investigations of the Iron(III)-Catalyzed Carbonyl-Olefin Metathesis Reaction. *J. Am. Chem. Soc.* **2017**, *139* (31), 10832−10842.
(18) Demole, E.; Enggist, P.; Borer, M. C. Applications synthétiques de la cyclisation d'alcools tertiaires γ-éthyléniques en α-bromotétrahydrofurannes sous l'action du N-bromosuccinimide. II. Cyclisation du (±)-nérolidol en diméthyl-2,5-(méthyl-4-pentène-3-yl)-2-cycloheptène-4-one, tétraméthyl-3, 3, 7, 10-oxa-2-tricyclo[5.5.0.01,4]-dodécène-9, β-acoratriène, cédradiène-2,8, épi-2-α-cédrène et α-cédrène. *Helv. Chim. Acta* **1971**, *54* (7), 1845−1864.
(19) Miles, R. B.; Davis, C. E.; Coates, R. M. Syn- and Anti-Selective Prins Cyclizations of delta,epsilon-Unsaturated Ketones to 1,3-Halohydrins with Lewis Acids. *J. Org. Chem.* **2006**, *71* (4), 1493−1501.
(20) Coates and co-workers propose a different mechanism for their oxetane, which does not overlap with carbonyl-olefin metathesis.
(21) Kozuch, S.; Shaik, S. How to conceptualize catalytic cycles? The energetic span model. *Acc. Chem. Res.* **2011**, *44* (2), 101−110.
(22) Hansch, C.; Leo, A. *Substituent Constants for Correlation Analysis in Chemistry and Biology*; Wiley, 1979.
(23) Baker, J. W.; Nathan, W. S. 429. The mechanism of aromatic side-chain reactions with special reference to the polar effects of substituents. Part V. The polar effects of alkyl groups. *J. Chem. Soc.* **1935**, 1844−1847.
(24) Mulliken, R. S.; Rieke, C. A.; Brown, W. G. Hyperconjugation*. *J. Am. Chem. Soc.* **1941**, *63* (1), 41−56.
(25) Hyperconjugation. In *IUPAC Compendium of Chemical Terminology*, 3rd ed.; International Union of Pure and Applied Chemistry, 2006.
(26) Reed, A. E.; Weinhold, F. Natural localized molecular orbitals. *J. Chem. Phys.* **1985**, *83*, 1736−1740.
(27) Rasul, G.; Chen, J. L.; Prakash, G. K.; Olah, G. A. Ab initio/DFT/GIAO-CCSD(T) calculational study of the t-butyl cation: comparison of experimental data with structures, energetics, IR vibrational frequencies, and 13C NMR chemical shifts indicating preferred C(s) conformation. *J. Phys. Chem. A* **2009**, *113* (24), 6795−6799.
(28) Bull, J. A.; Croft, R. A.; Davis, O. A.; Doran, R.; Morgan, K. F. Oxetanes: Recent Advances in Synthesis, Reactivity, and Medicinal Chemistry. *Chem. Rev.* **2016**, *116* (19), 12150−12233.

https://doi.org/10.1021/acsomega.4c09880
ACS Omega 2025, 10, 10283−10293